



UNIVERSITY
OF TRENTO

DIPARTIMENTO DI INGEGNERIA E SCIENZA DELL'INFORMAZIONE

38123 Povo – Trento (Italy), Via Sommarive 14
<http://www.disi.unitn.it>

A MULTI-RESOLUTION TECHNIQUE BASED ON SHAPE
OPTIMIZATION FOR THE RECONSTRUCTION OF
HOMOGENEOUS DIELECTRIC OBJECTS

M. Benedetti, D. Lesselier, M. Lambert, and A. Massa

January 2009

Technical Report # DISI-11-032

A Multi-Resolution Technique based on Shape Optimization for the Reconstruction of Homogeneous Dielectric Objects

M. Benedetti^{1,2}, D. Lesselier², M. Lambert², and A. Massa¹

¹ Department of Information Engineering and Computer Science, *ELEDIA* Research Group, University of Trento, Via Sommarive 14, 38050 Trento - Italy, Tel. +39 0461 882057, Fax. +39 0461 882093

²Département de Recherche en Électromagnétisme - Laboratoire des Signaux et Systèmes, CNRS-SUPELEC Univ. Paris Sud 11, 3 rue Joliot-Curie, 91192 Gif-sur-Yvette CEDEX, France

E-mail: *manuel.benedetti@disi.unitn.it*, *lesselier@lss.supelec.fr*, *lambert@lss.supelec.fr*, *andrea.massa@ing.unitn.it*

Abstract. In the framework of inverse scattering techniques, this paper presents the integration of a multi-resolution technique and the level-set method for qualitative microwave imaging. On one hand, in order to effectively exploit the limited amount of information collectable from scattering measurements, the iterative multi-scaling approach (*IMSA*) is employed for enabling a detailed reconstruction only where needed without increasing the number of unknowns. On the other hand, the *a-priori* information on the homogeneity of the unknown object is exploited by adopting a shape-based optimization and representing the support of the scatterer via a level set function. Reliability and effectiveness of the proposed strategy are assessed by processing both synthetic and experimental scattering data for simple and complex geometries, as well.

Key Words - Microwave Imaging, Inverse Scattering, Level Sets, Iterative Multi-Scaling Approach, Homogeneous Dielectric Scatterers.

Classification Numbers (MSC) - 45Q05, 78A46, 78M50

1. Introduction

The non-invasive reconstruction of position and shape of unknown targets is a topic of great interest in many applications, such as non-destructive evaluation and testing (NDE/NDT) for industrial monitoring and subsurface sensing [1]. In this framework, many methodologies have been proposed based on x-rays [2], ultrasonics [3], and eddy currents [4]. Furthermore, microwave imaging has been recognized as a suitable methodology since [1][5]: (a) electromagnetic fields at microwave frequencies can penetrate non-ideal conductor materials; (b) the field scattered by the target is representative of its inner structure and not only of its boundary; (c) microwaves show a high sensibility to the water content of the structure under test; (d) microwave sensors can be employed without mechanical contacts with the specimen. In addition, compared to x-ray and magnetic resonance, microwave-based approaches minimize (or avoid) collateral effects in the specimen under test. Therefore, they can be safely employed in biomedical imaging.

A further advance in microwave non-invasive inspection is represented by inverse scattering approaches aimed at reconstructing a complete image of the region under test. Unfortunately, the underlying mathematical model is characterized by several drawbacks preventing their massive employment in NDE/NDT applications. In particular, inverse scattering problems are intrinsically ill-posed [6] as well as non-linear [7].

Since the ill-posedness is strongly related to the amount of collectable information and usually the number of independent data is lower than the dimension of the solution space, multi-view/multi-illumination systems are generally adopted. However, it is well known that the collectable information is an upper-bounded quantity [8]-[10]. Consequently, it is necessary to effectively exploit the overall information contained in the scattered field samples for achieving a satisfactory reconstruction.

Towards this end, multi-resolution strategies have been recently proposed. The idea is that of using an enhanced spatial resolution only in those regions where the unknown scatterers are found to be located. Accordingly, Miller *et al.* [11] proposed a statistically-based method for determining the optimal resolution level, while Baussard *et al.* [12] developed a strategy based on spline pyramids for sub-surface imaging problems. As for an example concerned with qualitative microwave imaging, Li *et al.* [13] implemented a multiscale technique based on Linear Sampling Method (LSM) to effectively reconstruct the contour of the scatterers. Unlike [11]-[13], the iterative multi-scale approach (IMSA)

developed by Caorsi *et al.* [14] performs a multi-step, multi-resolution inversion process in which the ratio between unknowns and data is kept suitably low and constant at each step of the inversion procedure, thus reducing the risk of occurrence of local minima [9] in the arising optimization problem.

On the other hand, the lack of information affecting the inverse problem has been addressed through the exploitation of the *a-priori* knowledge (when available) on the scenario under test by means of an effective representation of the unknowns. As far as many NDE/NDT applications are concerned, the unknown defect is characterized by known electromagnetic properties (i.e., dielectric permittivity and conductivity) and it lies within a known host region. Under these assumptions, the imaging problem reduces to a shape optimization problem aimed at the search of location and boundary contours of the defect. Parametric techniques aimed at representing the unknown object in terms of descriptive parameters of reference shapes [15][16] and more sophisticated approaches such as evolutionary-controlled spline curves [17][18], shape gradients [19]-[21] or level-sets [22]-[30] have then been proposed. As far as level-set-based methods are concerned, the homogeneous object is defined as the zero level of a continuous function and, unlike pixel-based or parametric-based strategies, such a description enables one to represent complex shapes in a simple way.

In order to exploit both the available *a-priori* knowledge on the scenario under test (e.g., the homogeneity of the scatterer) and the information content from the scattering measurements, this paper proposes the integration of the iterative multi-scaling strategy (*IMSA*) [14] and the level-set (*LS*) representation [23].

The paper is structured as follows. The integration between *IMSA* and *LS* is detailed in Sect. 2 dealing with a two-dimensional geometry. In Section 3, numerical testing and experimental validation are presented, a comparison with the standard *LS* implementation being made. Finally, some conclusions are drawn (Sect. 4).

2. Mathematical Formulation

Let us consider a cylindrical homogeneous non-magnetic object with relative permittivity ϵ_C and conductivity σ_C that occupies a region Υ belonging to an investigation domain D_I . Such a scatterer is probed by a set of V transverse-magnetic (*TM*) plane waves, with electric field directed along the axis of the cylindrical geometry,

namely $\underline{\zeta}^v(\underline{r}) = \zeta^v(\underline{r})\hat{\underline{z}}$ ($v = 1, \dots, V$), $\underline{r} = (x, y)$. The scattered field, $\underline{\xi}^v(\underline{r}) = \xi^v(\underline{r})\hat{\underline{z}}$, is collected at $M(v)$, $v = 1, \dots, V$, measurement points \underline{r}_m distributed in the observation domain D_O .

In order to electromagnetically describe the investigation domain D_I , let us define the contrast function $\tau(\underline{r})$ given by

$$\tau(\underline{r}) = \begin{cases} \tau_C & \underline{r} \in \Upsilon \\ 0 & \text{otherwise} \end{cases} \quad (1)$$

where $\tau_C = (\epsilon_C - 1) - j\frac{\sigma_C}{2\pi f\epsilon_0}$, f being the frequency of operation (the time dependence $e^{j2\pi ft}$ being implied).

The scattering problem is described by the well-known Lippmann-Schwinger integral equations

$$\xi^v(\underline{r}_m) = \left(\frac{2\pi}{\lambda}\right)^2 \int_{D_I} \tau(\underline{r}') E^v(\underline{r}') G_{2D}(\underline{r}_m, \underline{r}') d\underline{r}', \quad \underline{r}_m \in D_O \quad (2)$$

$$\zeta^v(\underline{r}) = E^v(\underline{r}) - \left(\frac{2\pi}{\lambda}\right)^2 \int_{D_I} \tau(\underline{r}') E^v(\underline{r}') G_{2D}(\underline{r}, \underline{r}') d\underline{r}', \quad \underline{r} \in D_I \quad (3)$$

where λ is the background wavelength, E^v is the total electric field, and $G_{2D}(\underline{r}, \underline{r}') = -\frac{j}{4}H_0^{(2)}\left(\frac{2\pi}{\lambda}\|\underline{r} - \underline{r}'\|\right)$ is the free-space two-dimensional Green's function, $H_0^{(2)}$ being the second-kind, zeroth-order Hankel function.

In order to retrieve the unknown position and shape of the target Υ by step-by-step enhancing the spatial resolution only in that region, called region-of-interest (*RoI*), $R \in D_I$, where the scatterer is located [14], the following iterative procedure of S_{max} steps is carried out.

With reference to Fig. 1(a) and to the block diagram displayed in Fig. 2, at the first step ($s = 1$, s being the step number) a trial shape $\Upsilon_s = \Upsilon_1$, belonging to D_I , is chosen and the region of interest R_s [$R_{s=1} = D_I$] is partitioned into N_{IMSA} equal square sub-domains, where N_{IMSA} depends on the degrees of freedom of the problem at hand and it is computed according to the guidelines suggested in [9].

In addition, the level set function ϕ_s is initialized by means of a signed distance function defined as follows [23][25]:

$$\phi_s(\underline{r}) = \begin{cases} -\min_{b=1, \dots, B_s} \|\underline{r} - \underline{r}_b\| & \text{if } \tau(\underline{r}) = \tau_C \\ \min_{b=1, \dots, B_s} \|\underline{r} - \underline{r}_b\| & \text{if } \tau(\underline{r}) = 0 \end{cases} \quad (4)$$

where $\underline{r}_b = (x_b, y_b)$ is the b -th border-cell ($b = 1, \dots, B_s$) of $\Upsilon_{s=1}$.

Then, at each step s of the process ($s = 1, \dots, S_{max}$), the following optimization procedure is repeated (Fig. 2):

- **Problem Unknown Representation** - The contrast function is represented in terms of the level set function as follows

$$\tilde{\tau}_{k_s}(\underline{r}) = \sum_{i=1}^s \sum_{n_i=1}^{N_{IMSA}} \tau_{k_i} \mathcal{B}(\underline{r}_{n_i}) \quad \underline{r} \in D_I \quad (5)$$

where the index k_s indicates the k -th iteration at the s -th step [$k_s = 1, \dots, k_s^{opt}$], $\mathcal{B}(\underline{r}_{n_i})$ is a rectangular basis function whose support is the n -th sub-domain at the i -th resolution level [$n_i = 1, \dots, N_{IMSA}$, $i = 1, \dots, s$], and the coefficient τ_{k_i} is given by

$$\tau_{k_i} = \begin{cases} \tau_C & \text{if } \Psi_{k_i}(\underline{r}_{n_i}) \leq 0 \\ 0 & \text{otherwise} \end{cases} \quad (6)$$

letting

$$\Psi_{k_i}(\underline{r}_{n_i}) = \begin{cases} \phi_{k_i}(\underline{r}_{n_i}) & \text{if } i = s \\ \phi_{k_i^{opt}}(\underline{r}_{n_i}) & \text{if } (i < s) \text{ and } (\underline{r}_{n_i} \in R_i) \end{cases} \quad (7)$$

with $i = 1, \dots, s$ as in (5).

- **Field Distribution Updating** - Once $\tilde{\tau}_{k_s}(\underline{r})$ has been estimated, the electric field $E_{k_s}^v(\underline{r})$ is numerically computed according to a point-matching version of the Method of Moments (MoM) [31] as

$$\tilde{E}_{k_i}^v(\underline{r}_{n_i}) = \sum_{p_i=1}^{N_{IMSA}} \zeta^v(\underline{r}_{p_i}) \left[1 - \tilde{\tau}_{k_i}(\underline{r}_{p_i}) G_{2D}(\underline{r}_{n_i}, \underline{r}_{p_i}) \right]^{-1}, \quad (8)$$

$$\underline{r}_{n_i}, \underline{r}_{p_i} \in D_I$$

$$n_i = 1, \dots, N_{IMSA}.$$

- **Cost Function Evaluation** - Starting from the total electric field distribution (8), the reconstructed scattered field $\tilde{\xi}_{k_s}^v(\underline{r}_m)$ at the m -th measurement point, $m = 1, \dots, M(v)$, is updated by solving the following equation

$$\tilde{\xi}_{k_s}^v(\underline{r}_m) = \sum_{i=1}^s \sum_{n_i=1}^{N_{IMSA}} \tilde{\tau}_{k_i}(\underline{r}_{n_i}) \tilde{E}_{k_i}^v(\underline{r}_{n_i}) G_{2D}(\underline{r}_m, \underline{r}_{n_i}) \quad (9)$$

and the fit between measured and reconstructed data is evaluated by the multi-resolution cost function Θ defined as

$$\Theta \{ \phi_{k_s} \} = \frac{\sum_{v=1}^V \sum_{m=1}^{M(v)} \left| \tilde{\xi}_{k_s}^v(\underline{r}_m) - \xi_{k_s}^v(\underline{r}_m) \right|^2}{\sum_{v=1}^V \sum_{m=1}^{M(v)} \left| \xi_{k_s}^v(\underline{r}_m) \right|^2}. \quad (10)$$

- **Minimization Stopping** - The iterative process stops [i.e., $k_s^{opt} = k_s$ and $\tilde{\tau}_s^{opt} = \tilde{\tau}_{k_s}$] when: (a) a set of conditions on the stability of the reconstruction holds true or (b) when the maximum number of iterations is reached [$k_s = K_{max}$] or (c) when the

value of the cost function is smaller than a fixed threshold γ_{th} . As far as the stability of the reconstruction is concerned [condition (a)], the first corresponding stopping criterion is satisfied when, for a fixed number of iterations, K_τ , the maximum number of pixels which vary their value is smaller than a user defined threshold γ_τ according to the relationship

$$\max_{j=1,\dots,K_\tau} \left\{ \sum_{n_s=1}^{N_{IMSA}} \frac{|\tilde{\tau}_{k_s}(\underline{\mathbf{r}}_{n_s}) - \tilde{\tau}_{k_s-j}(\underline{\mathbf{r}}_{n_s})|}{\tau_C} \right\} < \gamma_\tau \cdot N_{IMSA}. \quad (11)$$

The second criterion, about the stability of the reconstruction, is satisfied when the cost function becomes stationary within a window of K_Θ iterations as follows:

$$\frac{1}{K_\Theta} \sum_{j=1}^{K_\Theta} \frac{\Theta\{\phi_{k_s}\} - \Theta\{\phi_{k_s-j}\}}{\Theta\{\phi_{k_s}\}} < \gamma_\Theta. \quad (12)$$

K_Θ being a fixed number of iterations and γ_Θ being user-defined thresholds;. When the iterative process stops, the solution $\tilde{\tau}_s^{opt}$ at the s -th step is selected as the one represented by the “best” level set function ϕ_s^{opt} defined as

$$\phi_s^{opt} = \arg \left[\min_{h=1,\dots,k_s^{opt}} (\Theta\{\phi_h\}) \right]. \quad (13)$$

- **Iteration Update** - The iteration index is updated [$k_s \rightarrow k_s + 1$];
- **Level Set Update** - The level set is updated according to the following Hamilton-Jacobi relationship

$$\phi_{k_s}(\underline{\mathbf{r}}_{n_s}) = \phi_{k_s-1}(\underline{\mathbf{r}}_{n_s}) - \Delta t_s \mathcal{V}_{k_s-1}(\underline{\mathbf{r}}_{n_s}) \mathcal{H}\{\phi_{k_s-1}(\underline{\mathbf{r}}_{n_s})\} \quad (14)$$

where $\mathcal{H}\{\cdot\}$ is the Hamiltonian operator [32][33] given as

$$\mathcal{H}^2\{\phi_{k_s}(\underline{\mathbf{r}}_{n_s})\} = \begin{cases} \max^2\{\mathcal{D}_{k_s}^{x-}; 0\} + \min^2\{\mathcal{D}_{k_s}^{x+}; 0\} + \\ \quad + \max^2\{\mathcal{D}_{k_s}^{y-}; 0\} + \min^2\{\mathcal{D}_{k_s}^{y+}; 0\} \\ \quad \text{if } \mathcal{V}_{k(s)}(\underline{\mathbf{r}}_{n(s)}) \geq 0 \\ \\ \min^2\{\mathcal{D}_{k_s}^{x-}; 0\} + \max^2\{\mathcal{D}_{k_s}^{x+}; 0\} + \\ \quad + \min^2\{\mathcal{D}_{k_s}^{y-}; 0\} + \max^2\{\mathcal{D}_{k_s}^{y+}; 0\} \\ \quad \text{otherwise} \end{cases} \quad (15)$$

and $\mathcal{D}_{k_s}^{x\pm} = \frac{\pm\phi_{k_s}(x_{n_s\pm 1}, y_{n_s}) \mp \phi_{k_s}(x_{n_s}, y_{n_s})}{l_s}$, $\mathcal{D}_{k_s}^{y\pm} = \frac{\pm\phi_{k_s}(x_{n_s}, y_{n_s\pm 1}) \mp \phi_{k_s}(x_{n_s}, y_{n_s})}{l_s}$. Δt_s is the time-step chosen as $\Delta t_s = \Delta t_1 \frac{l_s}{l_1}$ with Δt_1 to be set heuristically according to the literature [23], l_s being the cell-side at the s -th resolution level. \mathcal{V}_{k_s} is the velocity

function computed following the guidelines suggested in [23] by solving the adjoint problem of (8) in order to determine the adjoint field $\mathcal{F}_{k_s}^v$. Accordingly,

$$\mathcal{V}_{k_s}(\underline{r}_{n_s}) = -\Re \left\{ \frac{\sum_{v=1}^V \tau_C E_{k_s}^v(\underline{r}_{n_s}) \mathcal{F}_{k_s}^v(\underline{r}_{n_s})}{\sum_{v=1}^V \sum_{m=1}^{M(v)} |\mathcal{E}_{k_s}^v(\underline{r}_m)|^2} \right\}, \quad (16)$$

$$n_s = 1, \dots, N_{IMSA}$$

where \Re stands for the real part.

When the s -th minimization process terminates, the contrast function is updated [$\tilde{\tau}_s^{opt}(\underline{r}) = \tilde{\tau}_{k_{s-1}}(\underline{r})$, $\underline{r} \in D_I$ (5)] as well as the *RoI* [$R_s \rightarrow R_{s-1}$]. To do so, the following operations are carried out:

- **Computation of the Barycenter of the RoI** - the center of R_s of coordinates $(\tilde{x}_s^c, \tilde{y}_s^c)$ is determined by computing the center of mass of the reconstructed shapes as follows [14] [Fig. 1(b)]

$$\tilde{x}_s^c = \frac{\int_{D_I} x \tilde{\tau}_s^{opt}(\underline{r}) \mathcal{B}(\underline{r}) dx dy}{\int_{D_I} \tilde{\tau}_s^{opt}(\underline{r}) \mathcal{B}(\underline{r}) dx dy} \quad (17)$$

$$\tilde{y}_s^c = \frac{\int_{D_I} y \tilde{\tau}_s^{opt}(\underline{r}) \mathcal{B}(\underline{r}) dx dy}{\int_{D_I} \tilde{\tau}_s^{opt}(\underline{r}) \mathcal{B}(\underline{r}) dx dy}; \quad (18)$$

- **Estimation of the Size of the RoI** - the side L_s of R_s is computed by evaluating the maximum of the distance $\delta_c(\underline{r}) = \sqrt{(x - \tilde{x}_s^c)^2 + (y - \tilde{y}_s^c)^2}$ in order to enclose the scatterer, namely

$$\tilde{L}_s = \max_{\underline{r}} \left\{ 2 \times \frac{\tilde{\tau}_s^{opt}(\underline{r})}{\tau_C} \delta_c(\underline{r}) \right\}. \quad (19)$$

Once the *RoI* has been identified, the level of resolution is enhanced [$k_s \rightarrow k_{s-1}$] only in this region by discretizing R_s into N_{IMSA} sub-domains [Fig. 1(c)] and by repeating the minimization process until the synthetic zoom becomes stationary ($s = s_{opt}$), i.e.,

$$\left\{ \frac{|Q_{s-1} - Q_s|}{|Q_{s-1}|} \times 100 \right\} < \gamma_Q, \quad Q = \tilde{x}^c, \tilde{y}^c, \tilde{L} \quad (20)$$

γ_Q being a threshold set as in [14], or until a maximum number of steps ($s_{opt} = S_{max}$) is reached.

At the end of the multi-step process ($s = s_{opt}$), the problem solution is obtained as $\tilde{\tau}_s^{opt}(\underline{r}_{n_i}) = \tilde{\tau}_s^{opt}(\underline{r}_{n_i})$, $n_i = 1, \dots, N_{IMSA}$, $i = 1, \dots, s_{opt}$.

3. Numerical Validation

In order to assess the effectiveness of the *IMSA-LS* approach, a selected set of representative results concerned with both synthetic and experimental data is presented herein. The performances achieved are evaluated by means of the following error figures:

- *Localization Error* δ

$$\delta|_p = \frac{\sqrt{(\tilde{x}_s^c|_p - x^c|_p)^2 - (\tilde{y}_s^c|_p - y^c|_p)^2}}{\lambda} \times 100 \quad (21)$$

where $\underline{x}_c|_p = (x^c|_p, y^c|_p)$ is the center of the p -th true scatterer, $p = 1, \dots, P$, P being the number of objects. The average localization error $\langle \delta \rangle$ is defined as

$$\langle \delta \rangle = \frac{1}{P} \sum_{p=1}^P \delta|_p. \quad (22)$$

- *Area Estimation Error* Δ

$$\Delta = \left[\sum_{i=1}^I \frac{1}{N_{IMSA}} \sum_{n_i=1}^{N_{IMSA}} \mathcal{N}_{n_i} \right] \times 100 \quad (23)$$

where \mathcal{N}_{n_i} is equal to 1 if $\tilde{\tau}^{opt}(\underline{x}_{n_i}) = \tau(\underline{x}_{n_i})$ and 0 otherwise.

As far as the numerical experiments are concerned, the reconstructions have been performed by blurring the scattering data with an additive Gaussian noise characterized by a signal-to-noise-ratio (*SNR*)

$$SNR = 10 \log \frac{\sum_{v=1}^V \sum_{m=1}^{M(v)} |\zeta^v(\underline{x}_m)|^2}{\sum_{v=1}^V \sum_{m=1}^{M(v)} |\mu^{v,m}|^2} \quad (24)$$

$\mu^{v,m}$ being a complex Gaussian random variable with zero mean value.

3.1. Synthetic Data - Circular Cylinder

3.1.1. Preliminary Validation In the first experiment, a lossless circular off-centered scatterer of known permittivity $\epsilon_C = 1.8$ and radius $\rho = \lambda/4$ is located in a square investigation domain of side $L_D = \lambda$ [23]. $V = 10$ *TM* plane waves are impinging from the directions $\theta_v = 2\pi(v-1)/V$, $v = 1, \dots, V$, and the scattering measurements are collected at $M = 10$ receivers uniformly distributed on a circle of radius $\rho_O = \lambda$.

As far as the initialization of the *IMSA-LS* algorithm is concerned, the initial trial object Υ_1 is a disk with radius $\lambda/4$ and centered in D_I . The initial value of the time step is set to $\Delta t_1 = 10^{-2}$ as in [23]. The *RoI* is discretized in $N_{IMSA} = 15 \times 15$ sub-domains at each step of the iterative multi-resolution process. Concerning the

stopping criteria, the following configuration of parameters has been selected according to a preliminary calibration dealing with simple known scatterers and noiseless data: $S_{max} = 4$ (maximum number of steps), $\gamma^{\tilde{x}^c} = \gamma^{\tilde{y}^c} = 0.01$ and $\gamma^{\tilde{L}} = 0.05$ (multi-step process thresholds), $K_{max} = 500$ (maximum number of optimization iterations), $\gamma_{\Theta} = 0.2$ and $\gamma_{\tau} = 0.02$ (optimization thresholds), $K_{\Theta} = K_{\tau} = 0.15 K_{max}$ (stability counters), and $\gamma_{th} = 10^{-5}$ (threshold on the cost function).

Figure 3 shows samples of reconstructions with the *IMSA-LS*. At the first step [Fig. 3(a) - $s = 1$], the scatterer is correctly located, but its shape is only roughly estimated. Thanks to the multi-resolution representation, the qualitative imaging of the scatterer is improved in the next step [Fig. 3(b) - $s = s_{opt} = 2$] as confirmed by the error indexes in Tab. 1. For comparison purposes, the profile retrieved by the single-resolution method [23] (indicated in the following as *Bare-LS*), when D_I has been discretized in $N_{Bare} = 31 \times 31$ equal sub-domains, is shown [Fig. 3(c)]. In general, the discretization of the *Bare-LS* has been chosen in order to achieve in the whole investigation domain a reconstruction with the same level of spatial resolution obtained by the *IMSA-LS* in the *RoI* at $s = s_{opt}$.

Although the final reconstructions [Figs. 3(b)(c)] achieved by the two approaches are similar and quite close to the true scatterer sampled at the spatial resolution of *Bare-LS* [Fig. 3(d)] and *IMSA-LS* [Fig. 3(b)], the *IMSA-LS* more faithfully retrieves the symmetry of the actual object, even though the reconstruction error appears to be larger than the one of the *Bare-LS* (Fig. 4). During the iterative procedure, the cost function $\Theta_{opt} = \Theta \{ \phi_s^{opt} \}$ is initially characterized by a monotonically decreasing behavior. Then, $\Theta_{opt}|_{IMSA}$ becomes stationary until the stopping criterion defined by relationships (11) and (12) is satisfied (Fig. 4 - $s = 1$). Then, after the update of the field distribution inducing the error spike when $s = s_{opt} = 2$ and $k_s = 1$, $\Theta_{opt}|_{IMSA}$ settles to a value of 6.28×10^{-4} which is of the order of the *Bare-LS* error ($\Theta_{opt}|_{Bare} = 1.42 \times 10^{-4}$). Such a slight difference between $\Theta_{opt}|_{IMSA}$ and $\Theta_{opt}|_{Bare}$ depends on the different discretization [i.e., the basis functions $\mathcal{B}(\underline{r}_{n(i=2)})$, $n(i) = 1, \dots, N_{IMSA}$ are not the same as those of *Bare-LS*], but it does not affect the reconstruction in terms of both localization and area estimation, since $\delta|_{IMSA-LS} < \delta|_{Bare-LS}$ and $\Delta|_{IMSA-LS} < \Delta|_{Bare-LS}$ (Tab. 1).

Fig. 4 also shows that the multi-step multi-resolution strategy is characterized by a lower computational burden because of the smaller number of iterations for reaching the convergence (Fig. 4 - $k_{tot}|_{IMSA} = 125$ vs. $k_{tot}|_{Bare} = 177$, being k_{tot} the total number of iterations defined as $k_{tot} = \sum_{s=1}^{s_{opt}} k_s^{opt}$ for the *IMSA-LS*), and especially to the

reduced number of floating-point operations. As a matter of fact, since the complexity of the *LS*-based algorithms is of the order of $\mathcal{O}(2 \times \eta^3)$, $\eta = N_{IMSA}, N_{Bare}$ (i.e., the solution of two direct problems is necessary for computing an estimate of the scattered field and for updating the velocity vector), the computational cost of the *IMSA-LS* at each iteration is two orders in magnitude smaller than that of the *Bare-LS*.

3.1.2. Noisy Data As for the stability of the proposed approach, Figure 5 shows the reconstructions with the *IMSA-LS* [Figs. 5(a)(c)(e)] compared to those of the *Bare-LS* [Figs. 5(b)(d)(f)] with different levels of additive noise on the scattered data [$SNR = 20\text{ dB}$ (*top*); $SNR = 10\text{ dB}$ (*middle*); $SNR = 5\text{ dB}$ (*bottom*)]. As expected, when the *SNR* decreases, the performances worsen. However, as outlined by the behavior of the error figures in Tab. 2, blurred data and/or noisy conditions affect more evidently the *Bare* implementation than the multi-resolution approach. For completeness, the behavior of $\Theta_{opt}|_{IMSA}$ versus the iteration index is reported in Fig. 6 for different levels of *SNR*. As it can be noticed, the value of the error at the end of the iterative procedure decreases as the *SNR* increases.

In the second experiment, the same circular scatterer, but centered at a different position within a larger investigation square of side $L_D = 2\lambda$ ($\rho_O = 2\lambda$), has been reconstructed. According to [9], $M = 20$; $v = 1, \dots, V$ receivers and $V = 20$ views are considered and D_I is discretized in $N_{IMSA} = 13 \times 13$ pixels.

Figure 7(a) shows the reconstruction obtained at the convergence ($s_{opt} = 3$) by *IMSA-LS* when $SNR = 5\text{ dB}$. The result reached by the *Bare-LS* ($N_{BARE} = 47 \times 47$) is reported in Fig. 7(b) as well. As it can be noticed, the multi-resolution inversion is characterized by a better estimation of the object center and shape as confirmed by the values of δ and Δ ($\delta|_{IMSA-LS} = 0.59$ vs. $\delta|_{Bare-LS} = 2.72$ and $\Delta|_{IMSA-LS} = 0.48$ vs. $\Delta|_{Bare-LS} = 0.64$). As for the computational load, the same conclusions from previous experiments hold true.

3.2. Synthetic Data - Rectangular Scatterer

The second test case deals with a more complex scattering configuration. A rectangular off-centered scatterer ($L = 0.27\lambda$ and $W = 0.13\lambda$) characterized by a dielectric permittivity $\epsilon_C = 1.8$ is located within an investigation domain of $L_D = 3\lambda$ as indicated by the red dashed line in Fig. 8. In such a case, the imaging setup is made up of $V = 30$ sources and $M = 30$ measurement points for each view v [9]. D_I is partitioned into

$N_{IMSA} = 19 \times 19$ sub-domains (while $N_{Bare} = 33 \times 33$) and Δt_1 is set to 0.06.

3.2.1. Validation of the Stopping Criteria Before discussing the reconstruction capabilities, let us show a result concerned with the behavior of the proposed approach when varying the user-defined thresholds (γ_Θ , γ_τ , $\gamma_{\tilde{x}^c}$, $\gamma_{\tilde{y}^c}$, $\gamma_{\tilde{L}}$) of the stopping criteria. Figure 8 displays the reconstructions achieved by using the sets of parameters given in Tab. 3 [Γ_1 - Fig. 8(a); Γ_2 - Fig. 8(b); Γ_3 - Fig. 8(c); Γ_4 - Fig. 8(d)] while the behaviors of the cost function are depicted in Fig. 9. As it can be noticed, the total number of iterations k_{tot} increases as the values of the thresholds γ_Θ and γ_τ decrease. However, in spite of a larger k_{tot} , using lower threshold values does not provide better results, as shown by the comparison between settings Γ_2 and Γ_4 [Figs. 8(b)-(d), and Fig. 9]. The sets of parameters characterized by $\gamma_\Theta = 0.2$ and $\gamma_\tau = 0.02$ provide a good trade-off between the arising computational burden and the quality of the reconstructions. As far as the stopping criterion of the multi-resolution procedure is concerned, Figure 9 also shows two different behaviors of the cost function when using Γ_2 and Γ_3 (letting $\gamma_\Theta = 0.2$ and $\gamma_\tau = 0.02$). In particular, the proposed approach stops at $s_{opt} = 3$, instead of $s_{opt} = 4$, when increasing by a degree of magnitude the values of $\gamma_{\tilde{x}^c}$, $\gamma_{\tilde{y}^c}$, and $\gamma_{\tilde{L}}$. Although with a heavier computational burden, the choice $\gamma_{\tilde{x}^c} = \gamma_{\tilde{y}^c} = 0.01$ and $\gamma_{\tilde{L}} = 0.05$ results more effective [see Fig. 8(b) vs. Fig. 8(c)].

3.2.2. Noisy Data Figures 10-12 and Table 4 show the results from the comparative study carried out in correspondence with different values of signal-to-noise ratio [$SNR = 20 dB$ - Fig. 10(a) vs. Fig. 10(b); $SNR = 10 dB$ - Fig. 10(c) vs. Fig. 10(d); $SNR = 5 dB$ - Fig. 10(e) vs. Fig. 10(f)]. They further confirm the reliability and efficiency of the multi-resolution strategy in terms of qualitative reconstruction errors (Fig. 11), especially when the noise level grows. In particular, the *Bare* implementation does not yield either the position or the shape of the rectangular scatterer when $SNR = 5 dB$, whereas the *IMSA-LS* properly retrieves both the barycenter and the contour of the target. As for the computational cost, it should be noticed that although the *IMSA-LS* requires a greater number of iterations for reaching the convergence (Fig. 12, Tab. 4), the total amount of complex floating-point operations, $f_{pos} = \mathcal{O}(2 \times \eta^3) \times k_{tot}$, usually results smaller (Tab. 4).

3.3. Numerical Data - Hollow Cylinder

The third test case is concerned with the inversion of the data scattered by a higher permittivity ($\epsilon_C = 2.5$) off-centered cylindrical ring, letting $L_D = 3\lambda$. The external radius of the ring is $\rho_{ext} = \frac{2}{3}\lambda$, and the internal one is $\rho_{int} = \frac{\lambda}{3}$. By assuming the same arrangement of emitters and receivers as in Section 3.2, the investigation domain is discretized with $N_{IMSA} = 19 \times 19$ and $N_{Bare} = 35 \times 35$ square cells for the *IMSA-LS* and the *Bare-LS*, respectively. Moreover, Δt_1 is initialized to 0.003.

As it can be observed from Fig. 13, where the profiles when $SNR = 20\text{ dB}$ [Figs. 13(a)(b)] and $SNR = 10\text{ dB}$ [Figs. 13(c)(d)] reconstructed by means of the *IMSA-LS* [Figs. 13(a)(c)] and the *Bare-LS* [Figs. 13(b)(d)] are shown, the integrated strategy usually overcomes the standard one both in locating the object and in estimating the shape. In particular, when $SNR = 20\text{ dB}$, the distribution in Fig. 13(a) is a faithful estimate of the scatterer under test ($\delta]_{IMSA-LS} = 1.25$ and $\Delta]_{IMSA-LS} = 3.13$). On the contrary, the reconstruction with the *Bare-LS* is very poor ($\delta]_{Bare-LS} = 65.2$ and $\Delta]_{Bare-LS} = 34.39$). Certainly, a smaller SNR value impairs the inversion as shown in Fig. 13(c) [compared to Fig. 13(a)]. However, in this case, the *IMSA-LS* is able to properly locate the object ($\delta]_{IMSA-LS} = 1.7$ vs. $\delta]_{Bare-LS} = 65.9$) giving rough but useful indications about its shape ($\Delta]_{IMSA-LS} = 7.6$ vs. $\Delta]_{Bare-LS} = 34.55$).

3.4. Synthetic Data - Multiple Scatterers

The last synthetic test case is aimed at illustrating the behavior of the *IMSA-LS* when dealing with $P = 3$ scatterers ($\epsilon_C = 2.0$) distanced from one another. The test geometry is characterized by an elliptic off-centered cylinder, a circular off-centered scatterer, and a square off-centered object located in a square investigation domain characterized by $L_D = 3\lambda$. By adopting the same arrangement of emitters and receivers as in Section 3.3, the investigation domain is discretized with $N_{IMSA} = 23 \times 23$ and $N_{Bare} = 31 \times 31$ square cells for the *IMSA-LS* and the *Bare-LS*, respectively. Moreover, Δt_1 is set to 0.03.

Figures 14 and 15 show the results from the comparative study carried out in correspondence with different values of signal-to-noise ratio. As shown by the reconstructions (Fig. 14) and as expected, the multi-resolution approach provides more accurate results and appears to be more reliable than the *Bare-LS* especially with low SNR . This conclusion is further confirmed by the behavior of the reconstruction errors

(Fig. 15), for which the *IMSA-LS* achieves a lower localization error as well as a lower area error than those of *Bare-LS*, especially for $SNR = 5\text{ dB}$. On the other hand, both algorithms provide good estimates of the scatterer under test when inverting data affected by low noise [$SNR = 20\text{ dB}$ - Fig. 14(a) vs. Fig. 14(b); Fig. 15(a) and (b)].

3.5. Laboratory-Controlled Data

In order to further assess the effectiveness of the *IMSA-LS* also in dealing with experimental data, the multiple-frequency angular-diversity bi-static benchmark provided by *Institut Fresnel* in Marseille (France) has been considered. With reference to the experimental setup described in [34], the dataset “*dielTM_dec8f.exp*” has been processed. The field samples [$M = 49$, $V = 36$] are related to an off-centered homogeneous circular cylinder $\rho = 15\text{ mm}$ in diameter, characterized by a nominal value of the object function equal to $\tau(\underline{r}) = 2.0 \pm 0.3$, and located at $x_c = 0.0$, $y_c = -30\text{ mm}$ within an investigation domain assumed in the following of square geometry and extension $20 \times 20\text{ cm}^2$.

By setting $\epsilon_C = 3.0$, the reconstructions achieved are shown in Fig. 16 (*left column*) compared to those from the standard *LS* (*right column*) at $F = 4$ different operation frequencies. Whatever the frequency, the unknown scatterer is accurately localized and both algorithms yield, at convergence, structures that occupy a large subset of the true object. Such a similarity of performances, usually verified in synthetic experiments when the value of SNR is greater than 20 dB , seems to confirm the hypothesis of a low-noise environment as already evidenced in [35].

Finally, also in dealing with experimental datasets, the *IMSA-LS* proves its efficiency since the overall amount of complex floating point operations still remains two orders in magnitude lower than the one of the *Bare-LS* (Tab. 5 - Fig. 17).

4. Conclusions

In this paper, a multi-resolution approach for qualitative imaging purposes based on shape optimization has been presented. The proposed approach integrates the multi-scale strategy and the level set representation of the problem unknowns in order to profitably exploit the amount of information collectable from the scattering experiments as well as the available *a-priori* information on the scatterer under test.

The main key features of such a technique can be summarized as follows:

- innovative multi-level representation of the problem unknowns in the shape-deformation-based reconstruction technique;
- effective exploitation of the scattering data through the iterative multi-step strategy;
- limitation of the risk of being trapped in false solutions thanks to the reduced ratio between data and unknowns;
- useful exploitation of the *a-priori* information (i.e., object homogeneity) about the scenario under test;
- enhanced spatial resolution limited to the region of interest.

From the validation concerned with different scenarios and both synthetic and experimental data, the following conclusions can be drawn:

- the *IMSA-LS* usually proved more effective than the single-resolution implementation, especially when dealing with corrupted data scattered from simple as well as complex geometries characterized by one or several objects;
- the integrated strategy appeared less computationally-expensive than the standard approach in reaching a reconstruction with the same level of spatial resolution within the support of the object.

References

- [1] P. J. Shull, *Nondestructive Evaluation: Theory, Techniques and Applications*. CRC Press, 2002.
- [2] J. Baruchel, J.-Y. Buffière, E. Maire, P. Merle, and G. Peix, *X-Ray Tomography in Material Science*. Hermes Science, 2000.
- [3] L. W. Schmerr, *Fundamentals of Ultrasonic Nondestructive Evaluation: A Modeling Approach*. Springer, 1998.
- [4] B. A. Auld and J. C. Moulder, "Review of advances in quantitative eddy current nondestructive evaluation", *J. Nondestructive Evaluation*, vol. 18, no. 1, pp. 3-36, Mar. 1999.
- [5] R. Zoughi, *Microwave Nondestructive Testing and Evaluation*. Dordrecht, The Netherlands: Kluwer Academic Publishers, 2000.
- [6] O. M. Bucci and T. Isernia, "Electromagnetic inverse scattering: retrievable information and measurement strategies," *Radio Sci.*, vol. 32, pp. 2123-2138, Nov.-Dec. 1997.
- [7] M. Bertero and P. Boccacci, *Introduction to Inverse Problems in Imaging*. IOP Publishing Ltd, Bristol, 1998.
- [8] O. M. Bucci and G. Franceschetti, "On the spatial bandwidth of scattered fields," *IEEE Trans. Antennas Propagat.*, vol. 35, no. 12, pp. 1445-1455, Dec. 1987.
- [9] T. Isernia, V. Pascazio, and R. Pierri, "On the local minima in a tomographic imaging technique," *IEEE Trans. Antennas Propagat.*, vol. 39, no. 7, pp. 1696-1607, Jul. 2001.
- [10] H. Haddar, S. Kusiak, and J. Sylvester, "The convex back-scattering support," *SIAM J. Appl. Math.*, vol. 66, pp. 591-615, Dec. 2005.
- [11] E. L. Miller, and A. S. Willsky, "A multiscale, statistically based inversion scheme for linearized inverse scattering problems," *IEEE Trans. Antennas Propagat.*, vol. 34, no. 2, pp. 346-357, Mar. 1996.
- [12] A. Baussard, E. L. Miller, and D. Lesselier, "Adaptive multiscale reconstruction of buried objects," *Inverse Problems*, vol. 20, pp. S1-S15, Dec. 2004.
- [13] J. Li, H. Liu, and J. Zou, "Multilevel linear sampling method for inverse scattering problems," *SIAM J. Appl. Math.*, vol. 30, pp. 1228-1250, Mar. 2008.
- [14] S. Caorsi, M. Donelli, and A. Massa, "Detection, location, and imaging of multiple scatterers by means of the iterative multiscale method," *IEEE Trans. Microwave Theory Tech.*, vol. 52, no. 4, pp. 1217-1228, Apr. 2004.
- [15] S. Caorsi, A. Massa, M. Pastorino, and M. Donelli, "Improved microwave imaging procedure for nondestructive evaluations of two-dimensional structures," *IEEE Trans. Antennas Propagat.*, vol. 52, pp. 1386-1397, Jun. 2004.
- [16] M. Benedetti, M. Donelli, and A. Massa, "Multicrack detection in two-dimensional structures by means of GA-based strategies," *IEEE Trans. Antennas Propagat.*, vol. 55, no. 1, pp. 205-215, Jan. 2007.
- [17] V. Cingoski, N. Kowata, K. Kaneda, and H. Yamashita, "Inverse shape optimization using dynamically adjustable genetic algorithms," *IEEE Trans. Energy Conversion*, vol. 14, no. 3, pp. 661-666, Sept. 1999.
- [18] L. Lizzi, F. Viani, R. Azaro, and A. Massa, "Optimization of a spline-shaped UWB antenna by PSO," *IEEE Antennas Wireless Propagat. Lett.*, vol. 6, pp. 182-185, 2007.

-
- [19] J. Cea, S. Garreau, P. Guillame, and M. Masmoudi, "The shape and topological optimizations connection," *Comput. Methods Appl. Mech. Eng.*, vol. 188, no. 4, pp. 713-726, 2000.
- [20] G. R. Feijoo, A. A. Oberai, and P. M. Pinsky, "An application of shape optimization in the solution of inverse acoustic scattering problems," *Inverse Problems*, vol. 20, pp. 199-228, Feb. 2004.
- [21] M. Masmoudi, J. Pommier, and B. Samet, "The topological asymptotic expansion for the Maxwell equations and some applications," *Inverse Problems*, vol. 21, pp. 547-564, Apr. 2005.
- [22] F. Santosa, "A level-set approach for inverse problems involving obstacles," *ESAIM: COCV*, vol. 1, pp. 17-33, Jan. 1996.
- [23] A. Litman, D. Lesselier, and F. Santosa, "Reconstruction of a two-dimensional binary obstacle by controlled evolution of a level-set," *Inverse Problems*, vol. 14, pp. 685-706, Jun. 1998.
- [24] O. Dorn, E. L. Miller, C. M. Rappaport, "A shape reconstruction method for electromagnetic tomography using adjoint fields and level sets," *Inverse Problems*, vol. 16, pp. 1119-1156, May 2000.
- [25] C. Ramananjaona, M. Lambert, D. Lesselier, and J. P. Zolésio, "Shape reconstruction of buried obstacles by controlled evolution of a level-set: from a min-max formulation to a numerical experimentation," *Inverse Problems*, vol. 17, pp. 1087-1111, Dec. 2001.
- [26] R. Ferrayé, J.-Y. Dauvignac, and C. Pichot, "An inverse scattering method based on contour deformations by means of a level set method using frequency hopping technique," *IEEE Trans. Antennas Propagat.*, vol. 51, no. 5, pp. 1100-1113, May 2003.
- [27] E. T. Chung, T. F. Chan, X. C. Tai, "Electrical impedance tomography using level set representation and total variational regularization," *J. Comput. Phys.*, vol. 205, no. 2, pp. 707-723, May. 2005.
- [28] K. van den Doel and U. M. Asher, "Dynamic level set regularization for large distributed parameter estimation problems," *Inverse Problems*, vol. 23, pp. 1271-1288, Jun. 2007.
- [29] J. Strain, "Three methods for moving interfaces," *J. Comput. Phys.*, vol. 151, pp. 616-648, May 1999.
- [30] O. Dorn and D. Lesselier, "Level set methods for inverse scattering," *Inverse Problems*, vol. 22, pp. R67-R131, Aug. 2006.
- [31] J. H. Richmond, "Scattering by a dielectric cylinder of arbitrary cross-section shape," *IEEE Trans. Antennas Propagat.*, vol. 13, pp. 334-341, May 1965.
- [32] S. Osher and J. A. Sethian, "Fronts propagating with curvature-dependent speed: algorithms based on Hamilton-Jacobi formulations," *J. Comput. Phys.*, 79, pp. 12-49, Nov. 1988.
- [33] J. A. Sethian, *Level Set and Fast Marching Methods*. Cambridge University Press, Cambridge, UK, 2nd ed., 1999.
- [34] K. Belkebir and M. Saillard, "Testing inversion algorithms against experimental data," *Inverse Problems*, vol. 17, pp. 1565-1702, Dec. 2001.
- [35] M. Testorf and M. Fiddy, "Imaging from real scattered field data using a linear spectral estimation technique," *Inverse Problems*, vol. 17, pp. 1645-1658, Dec. 2001.

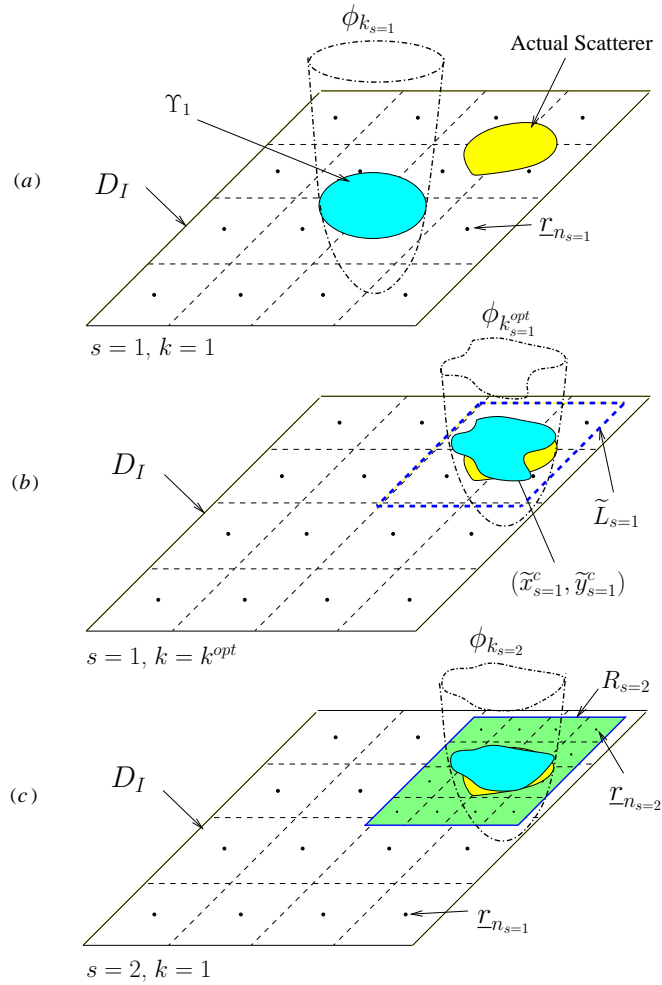


Figure 1. Graphical representation of the *IMSA-LS* zooming procedure. (a) First step ($k = 1$): the investigation domain is discretized in N sub-domains and a coarse solution is looked for. (b) First step ($k = k^{opt}$): the region of interest that contains the first estimate of the object is defined. (c) Second step ($k = 1$): an enhanced resolution level is used only inside the region of interest.

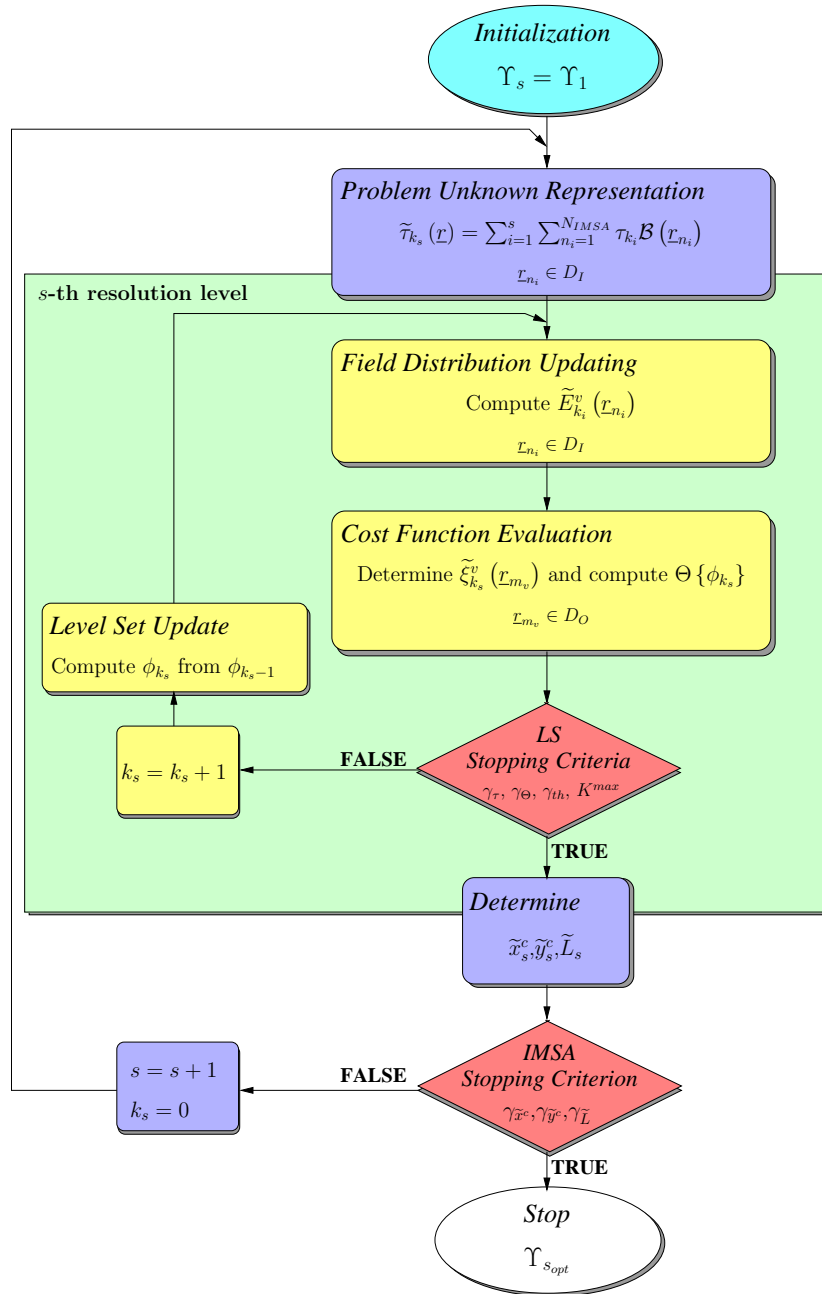


Figure 2. Block diagram description of the *IMSA-LS* zooming procedure.

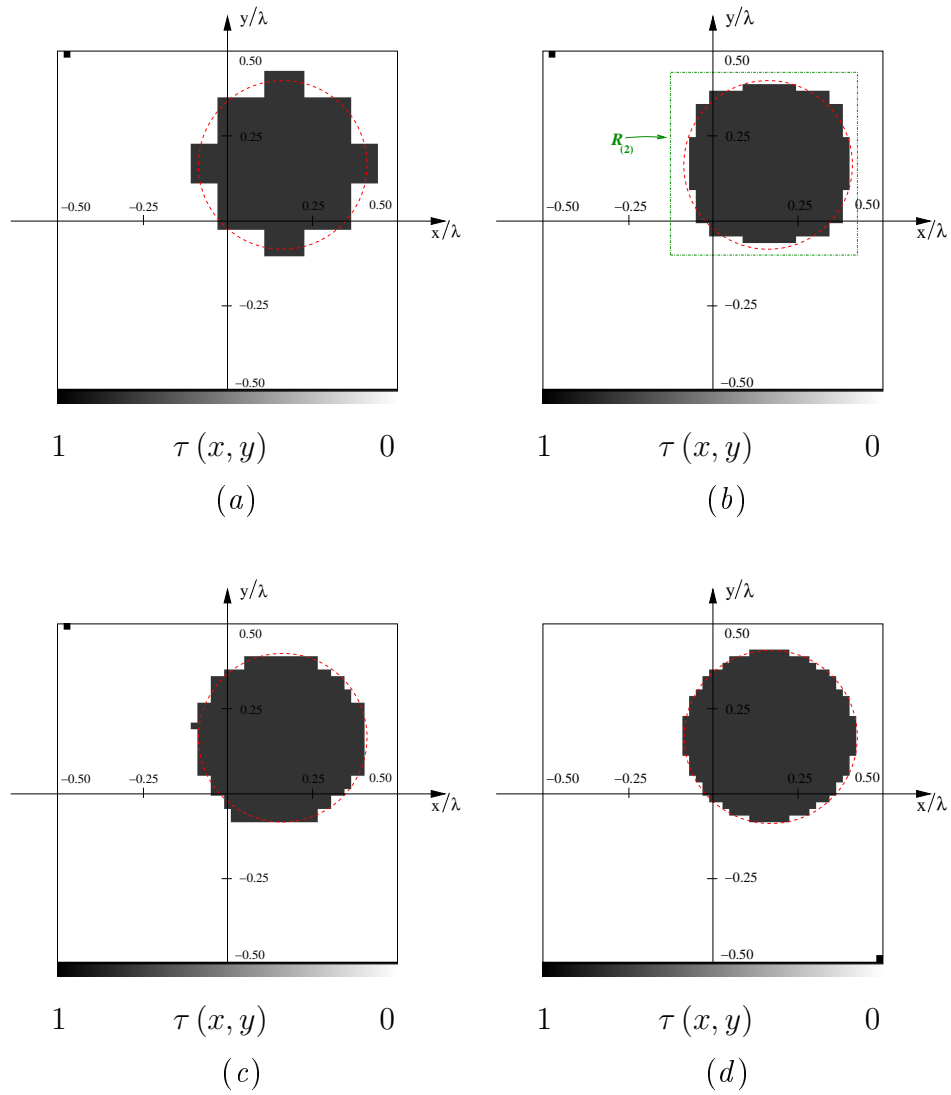


Figure 3. Numerical Data. Circular cylinder ($\epsilon_C = 1.8$, $L_D = \lambda$, *Noiseless Case*). Reconstructions with *IMSA-LS* at (a) $s = 1$ and (b) $s = s_{opt} = 2$, (c) *Bare-LS*. Optimal inversion (d).

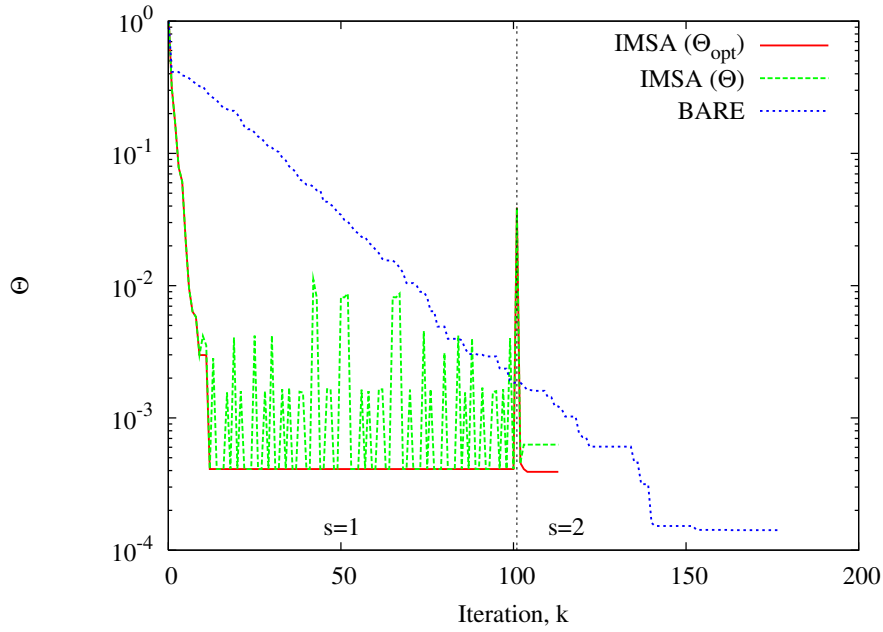


Figure 4. Numerical Data. Circular cylinder ($\epsilon_C = 1.8$, $L_D = \lambda$, *Noiseless Case*). Behavior of the cost function.

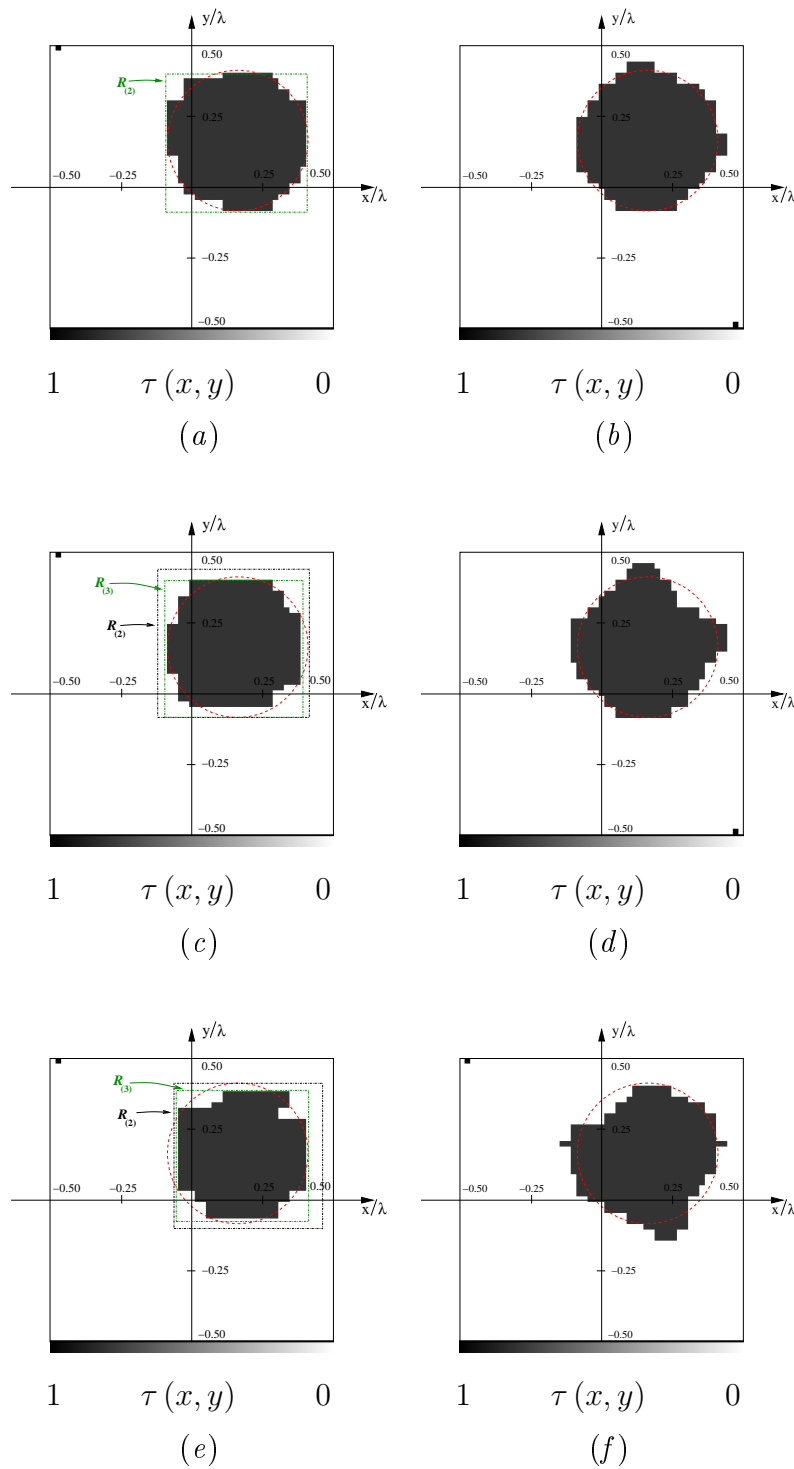


Figure 5. Circular cylinder ($\epsilon_C = 1.8$, $L_D = \lambda$, *Noisy Case*). Reconstructions with *IMSA-LS* (left column) and *Bare-LS* (right column) for different values of *SNR* [*SNR* = 20 dB (top), *SNR* = 10 dB (middle), *SNR* = 5 dB (bottom)].

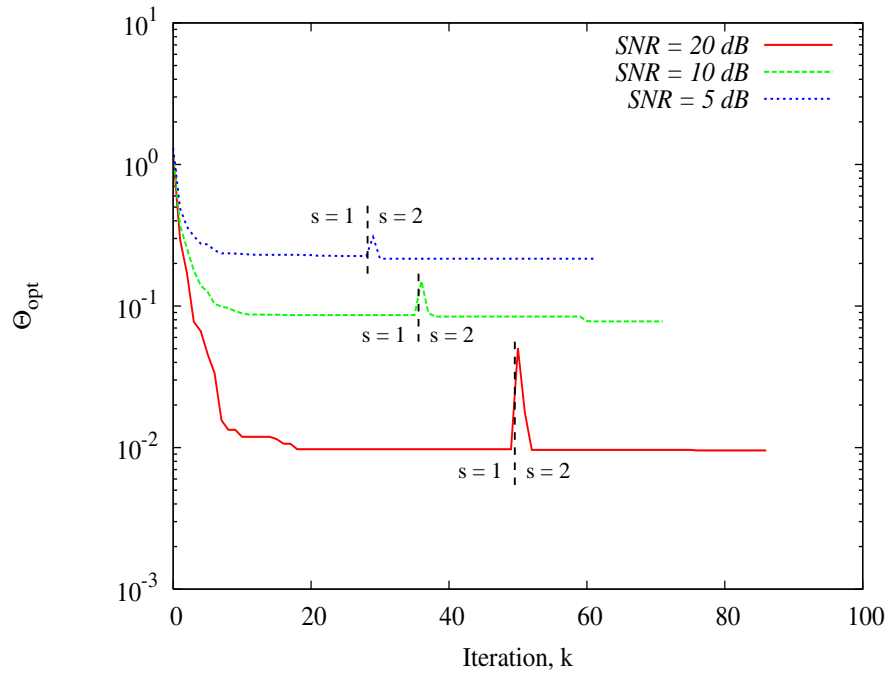


Figure 6. Numerical Data. Circular cylinder ($\epsilon_C = 1.8$, $L_D = \lambda$). Behavior of the cost function versus the noise level.

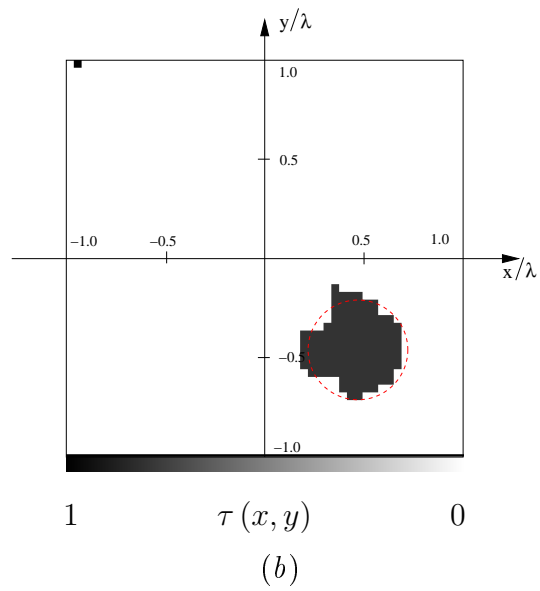
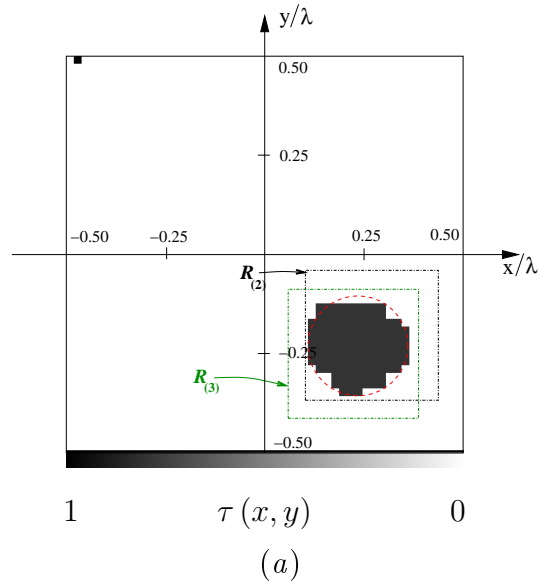


Figure 7. Numerical Data. Circular cylinder ($\epsilon_C = 1.8$, $L_D = 2\lambda$, $SNR = 5\text{ dB}$). Reconstructions with (a) *IMSA-LS* and (b) *Bare-LS*.

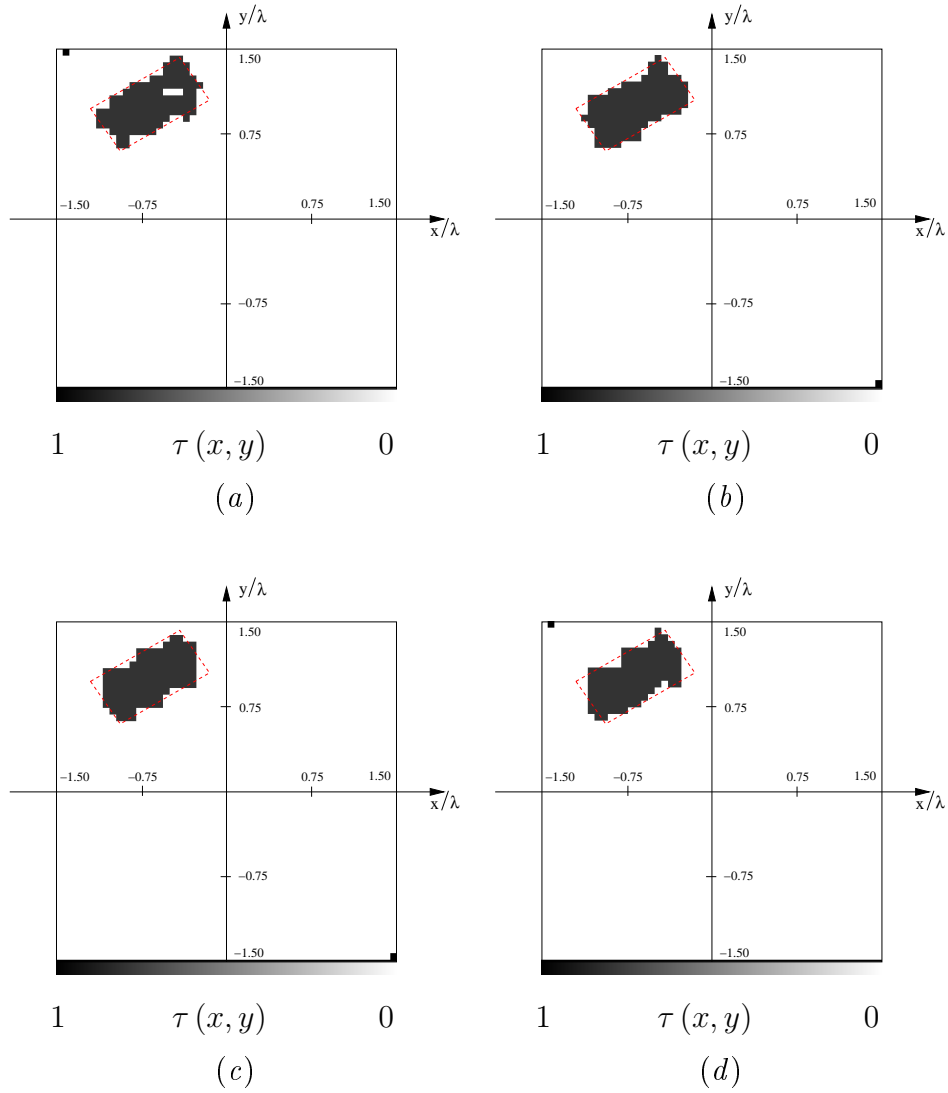


Figure 8. Numerical Data. Rectangular cylinder ($\epsilon_C = 1.8$, $L_D = 3\lambda$, *Noiseless Case*). Reconstructions with *IMSA-LS* for the different settings of Tab. 3 [(a) Γ_1 , (b) Γ_2 , (c) Γ_3 , (d) Γ_4].

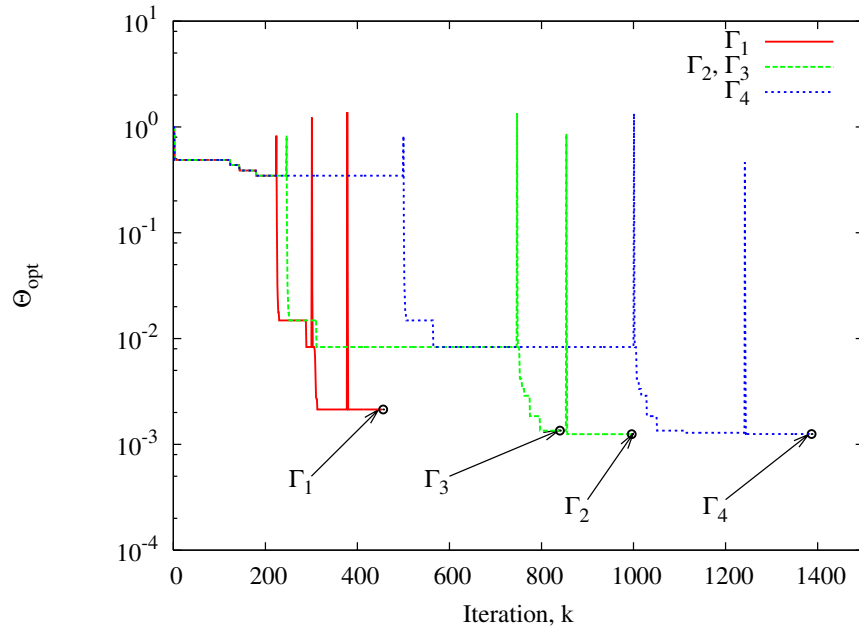


Figure 9. Numerical Data. Rectangular cylinder ($\epsilon_C = 1.8$, $L_D = 3\lambda$, *Noiseless Case*). Behavior of the cost function of *IMSA-LS* for the different settings of Tab. 3.

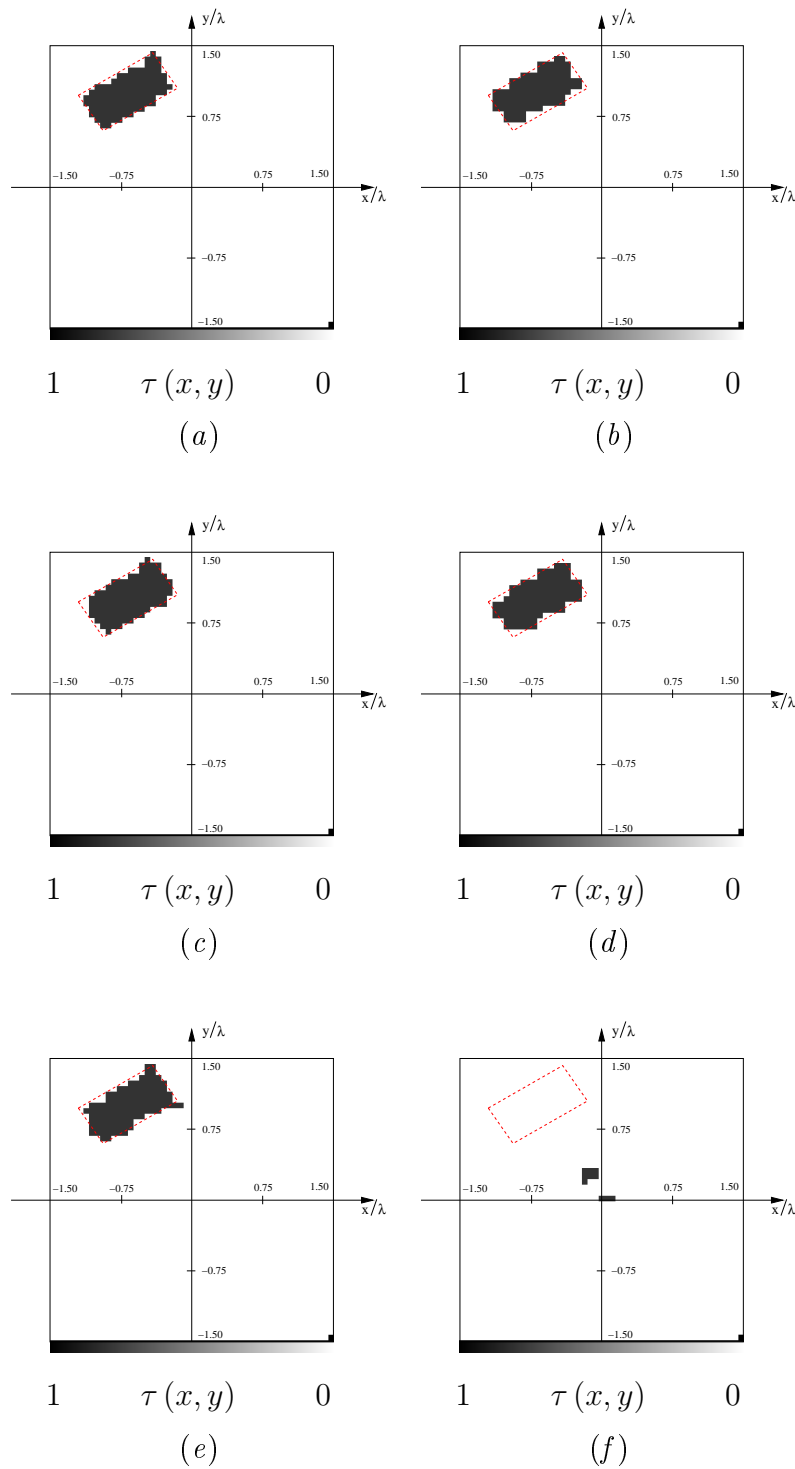
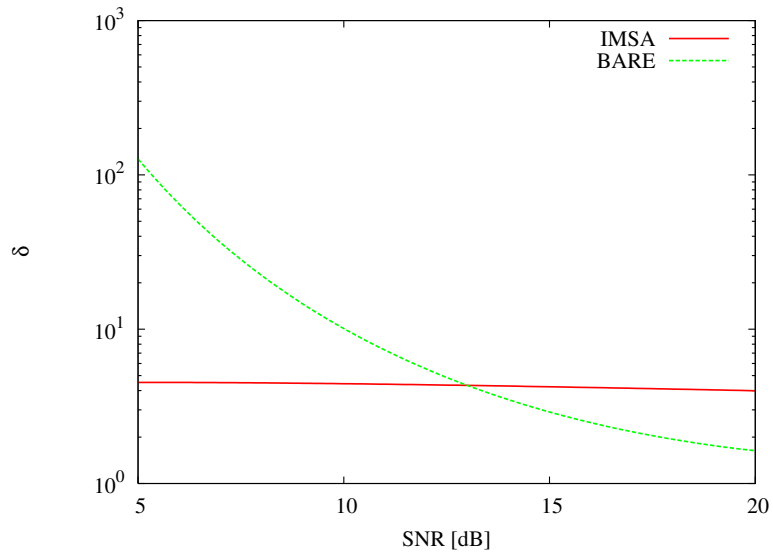
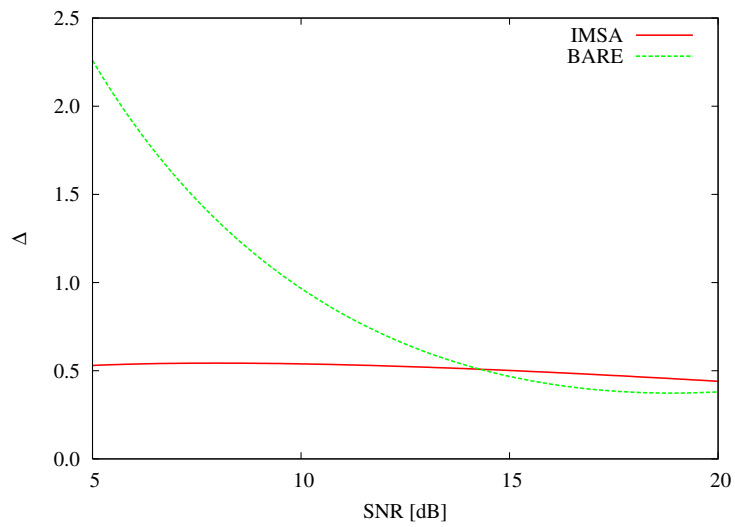


Figure 10. Numerical Data. Rectangular cylinder ($\epsilon_C = 1.8$, $L_D = 3\lambda$, *Noisy Case*). Reconstructions with *IMSA-LS* (left column) and *Bare-LS* (right column) for different values of *SNR* [*SNR* = 20 dB (top), *SNR* = 10 dB (middle), *SNR* = 5 dB (bottom)].

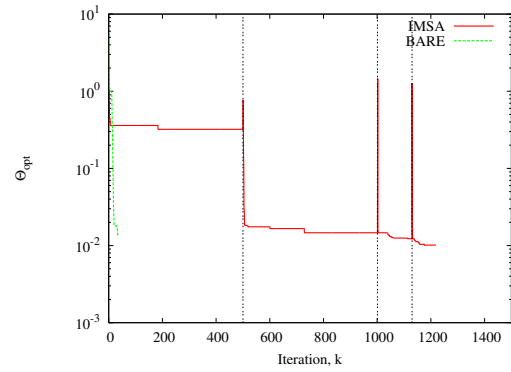


(a)

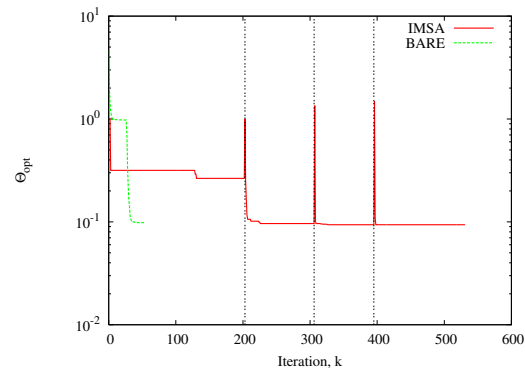


(b)

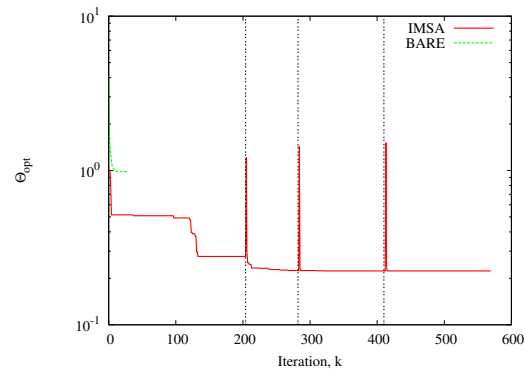
Figure 11. Numerical Data. Rectangular cylinder ($\epsilon_C = 1.8$, $L_D = 3\lambda$, *Noisy Case*). Values of the error figures versus SNR .



(a)



(b)



(c)

Figure 12. Numerical Data. Rectangular cylinder ($\epsilon_C = 1.8$, $L_D = 3\lambda$, *Noisy Case*). Behavior of the cost function versus the iteration index when (a) $SNR = 20\text{ dB}$, (b) $SNR = 10\text{ dB}$, and (c) $SNR = 5\text{ dB}$.

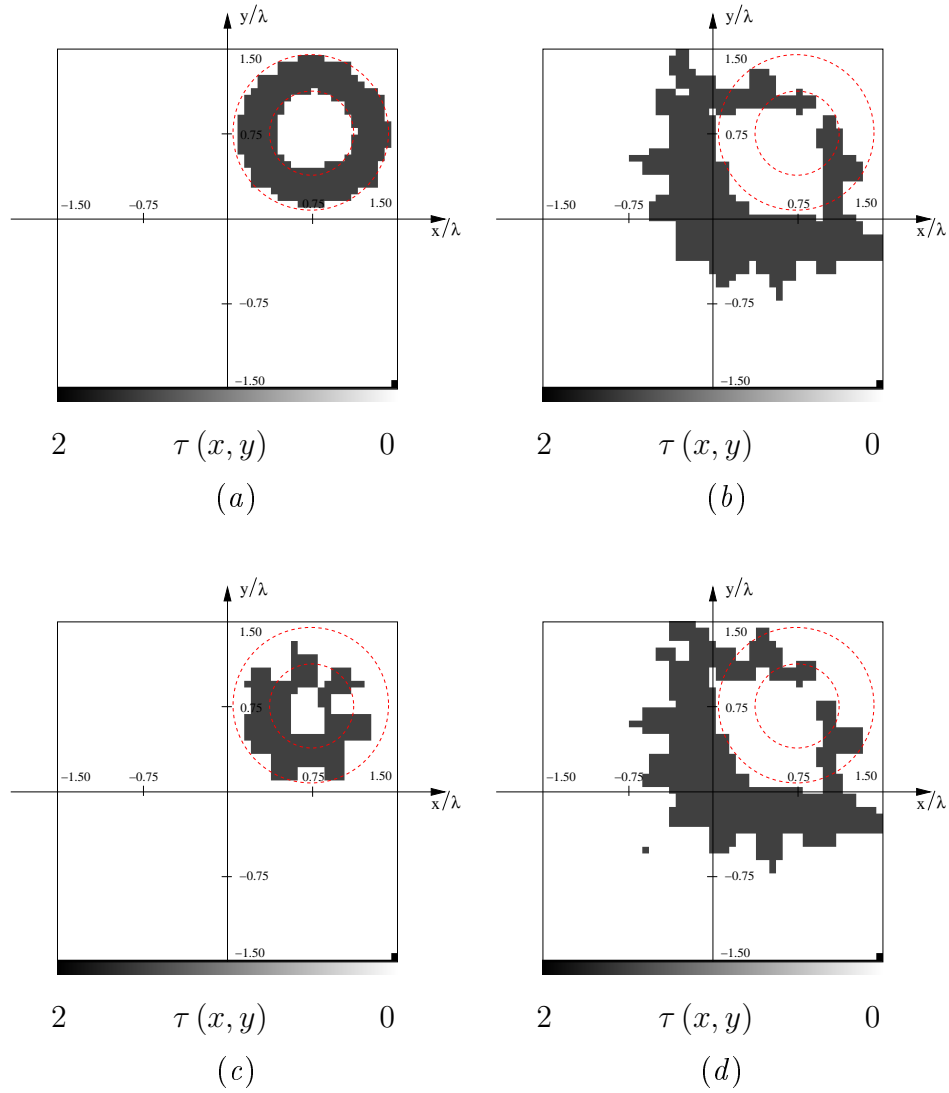


Figure 13. Numerical Data. Hollow cylinder ($\epsilon_C = 2.5$, $L_D = 3\lambda$, *Noisy Case*). Reconstructions with *IMSA-LS* (left column) and *Bare-LS* (right column) for different values of SNR [$SNR = 20 \text{ dB}$ (top), $SNR = 10 \text{ dB}$ (bottom)].

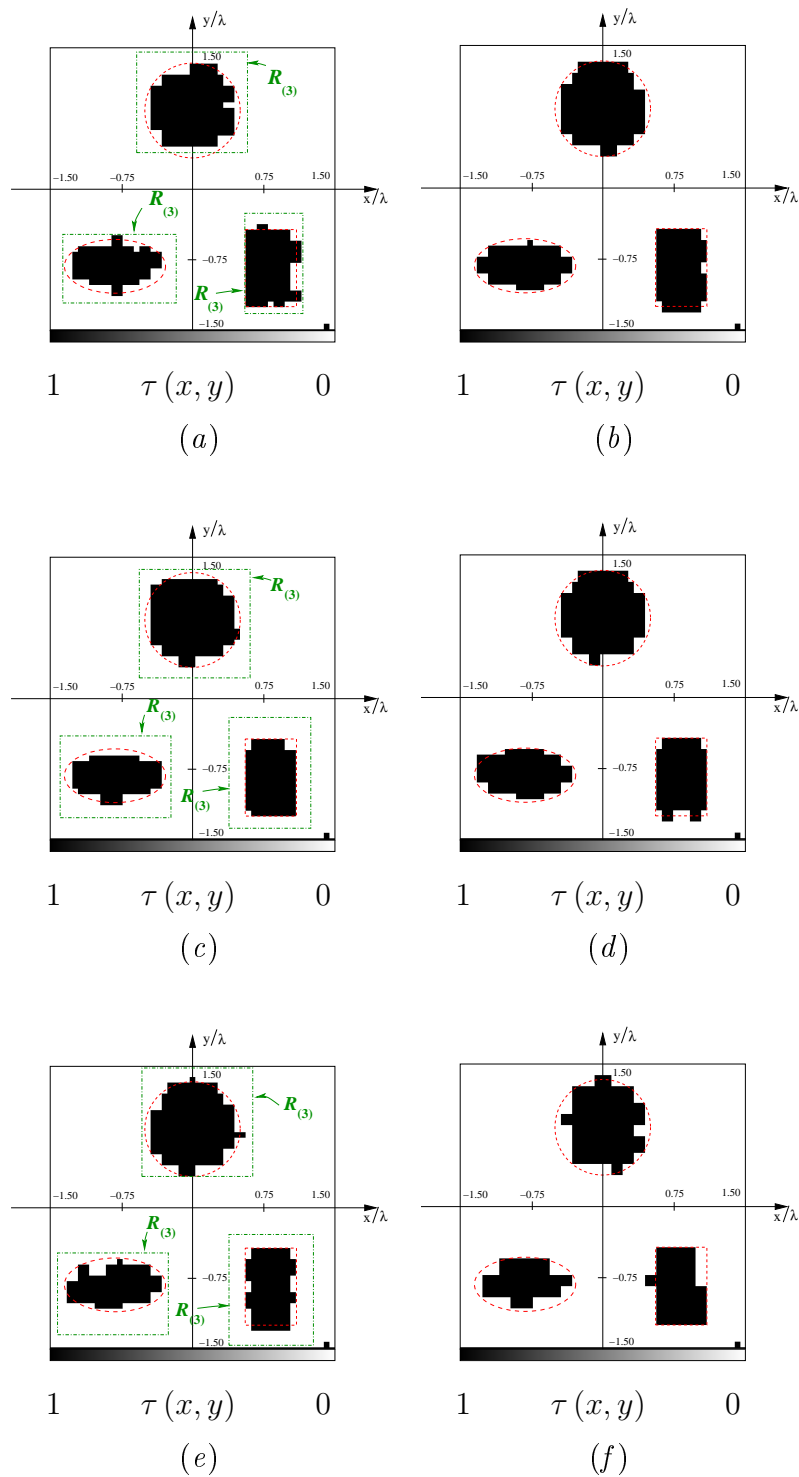
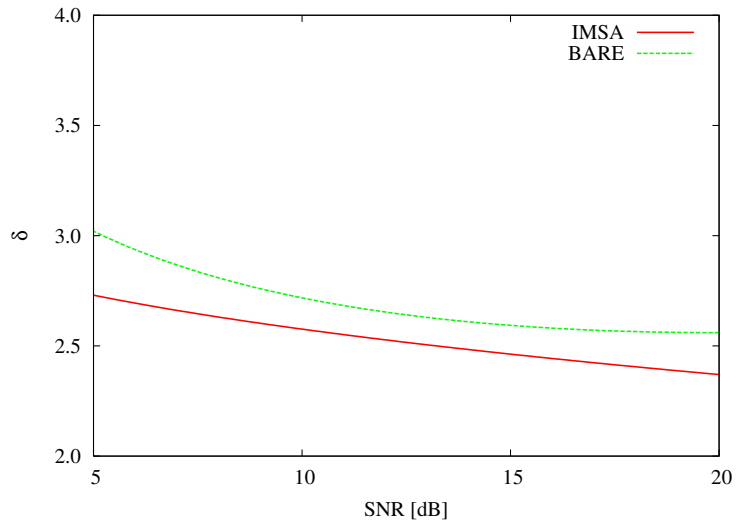
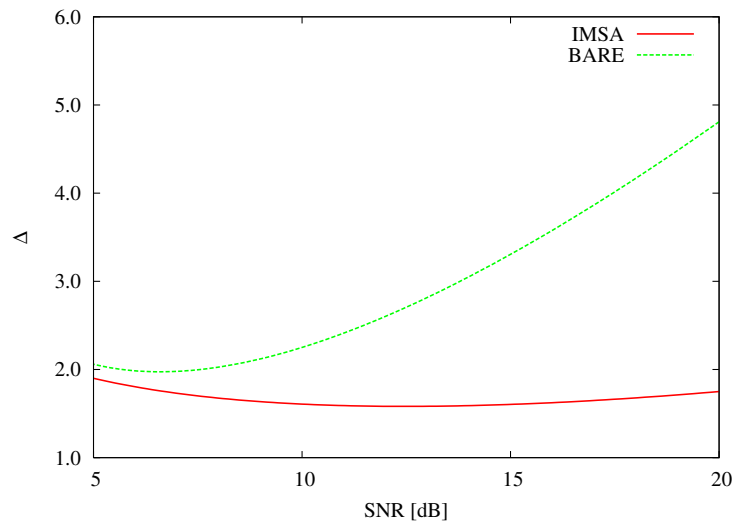


Figure 14. Numerical Data. Multiple scatterers ($\epsilon_C = 2.0$, $L_D = 3\lambda$, *Noisy Case*). Reconstructions with *IMSA-LS* (left column) and *Bare-LS* (right column) for different values of *SNR* [*SNR* = 20 dB (top), *SNR* = 10 dB (middle), *SNR* = 5 dB (bottom)].



(a)



(b)

Figure 15. Multiple scatterers ($\epsilon_C = 2.0$, $L_D = 3\lambda$, *Noisy Case*). Values of the error figures versus SNR .

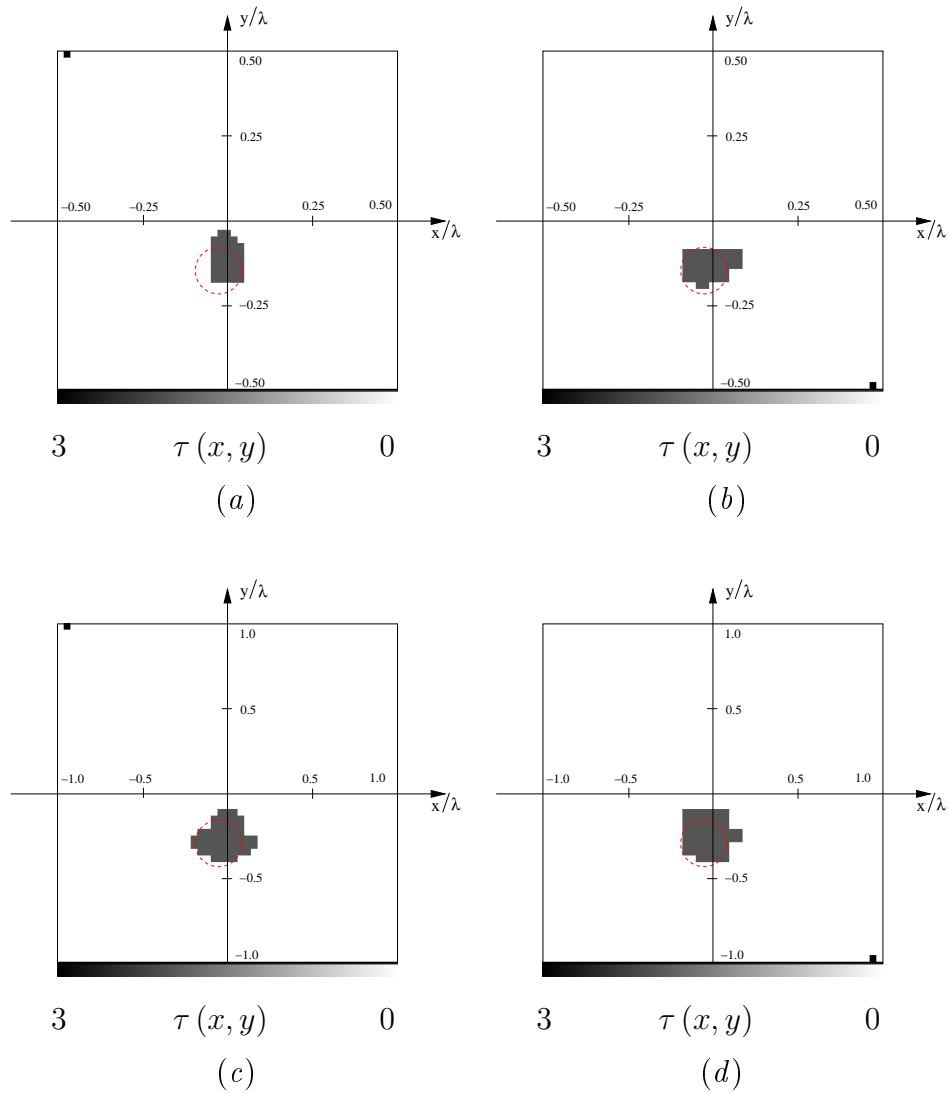


Figure 16(I). Experimental Data (Dataset “Marseille” [34]). Circular cylinder (“*dielTM_dec8f.exp*”). Reconstructions with *IMSA-LS* (left column) and *Bare-LS* (right column) at different frequencies f [$f = 1\text{ GHz}$ (a)(b); $f = 2\text{ GHz}$ (c)(d)].

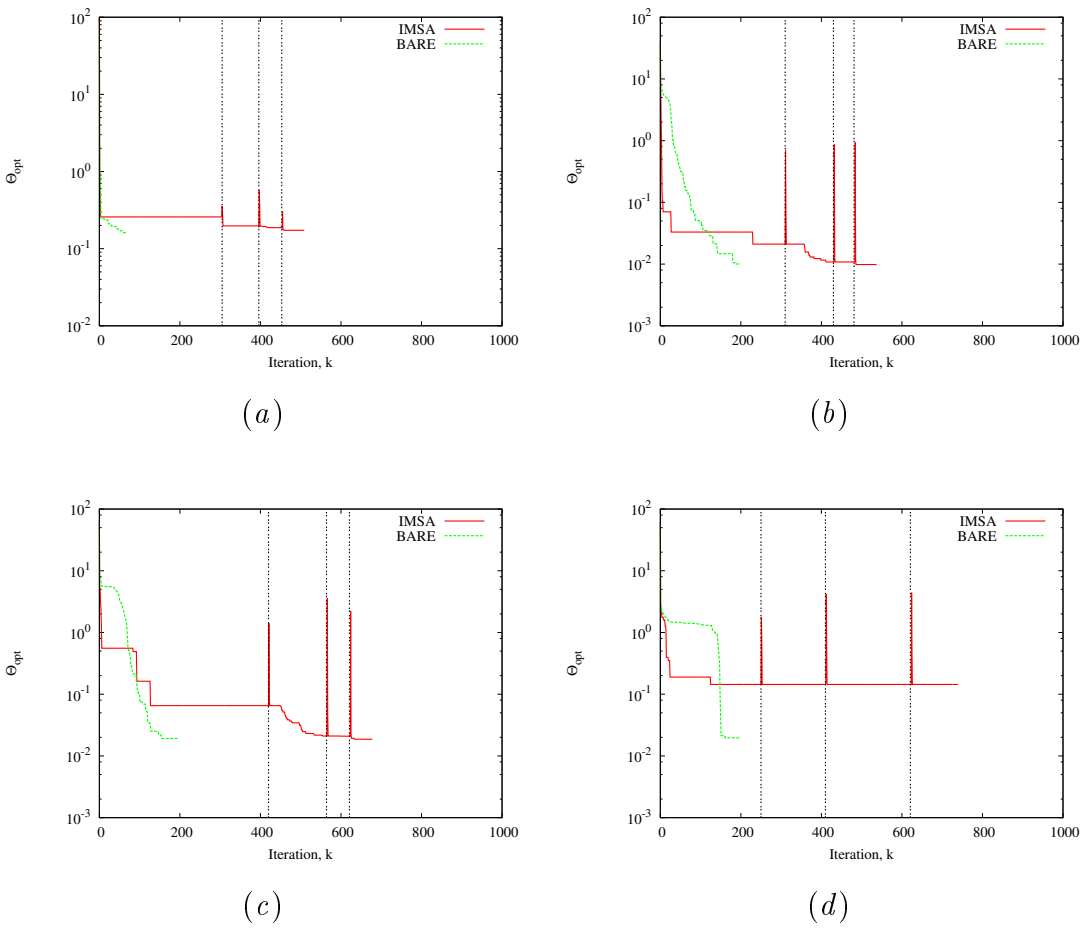


Figure 17. Experimental Data (Dataset “Marseille” [34]). Circular cylinder (“*delTM_dec8f.exp*”). Behavior of the cost function versus the number of iterations when (a) $f = 1 \text{ GHz}$, (b) $f = 2 \text{ GHz}$, (c) $f = 3 \text{ GHz}$, and (d) $f = 4 \text{ GHz}$.

	<i>IMSA - LS</i>		<i>Bare - LS</i>
	<i>s = 1</i>	<i>s = 2</i>	
δ	6.58×10^{-6}	2.19×10^{-6}	5.21×10^{-1}
Δ	2.36	0.48	0.64

Table 1. Numerical Data. Circular cylinder ($\epsilon_C = 1.8$, *Noiseless Case*). Error figures.

	<i>SNR = 20 dB</i>		<i>SNR = 10 dB</i>		<i>SNR = 5 dB</i>	
	<i>IMSA - LS</i>	<i>Bare - LS</i>	<i>IMSA - LS</i>	<i>Bare - LS</i>	<i>IMSA - LS</i>	<i>Bare - LS</i>
δ	5.91×10^{-1}	2.72	2.28	2.45	6.78×10^{-1}	1.63
Δ	0.98	1.28	1.07	1.80	1.50	2.07

Table 2. Numerical Data. Circular cylinder ($\epsilon_C = 1.8$, *Noisy Case*). Values of the error indexes for different values of *SNR*.

<i>Set of Parameters</i>	γ_Θ	γ_τ	$\gamma_{\tilde{x}^c}, \gamma_{\tilde{y}^c}$	$\gamma_{\tilde{L}}$
Γ_1	0.5	0.05	0.01	0.05
Γ_2	0.2	0.02	0.01	0.05
Γ_3	0.2	0.02	0.1	0.5
Γ_4	0.02	0.002	0.01	0.05

Table 3. Numerical Data. Rectangular cylinder ($\epsilon_C = 1.8$, $L_D = 3\lambda$, *Noiseless Case*). Different settings for the parameters of the stopping criteria.

	$SNR = 20\text{ dB}$		$SNR = 10\text{ dB}$		$SNR = 5\text{ dB}$	
	<i>IMSA - LS</i>	<i>Bare - LS</i>	<i>IMSA - LS</i>	<i>Bare - LS</i>	<i>IMSA - LS</i>	<i>Bare - LS</i>
k_{tot}	1089	41	393	53	410	28
N	361	1089	361	1089	361	1089
f_{pos}	1.02×10^{11}	1.02×10^{11}	3.70×10^{10}	1.37×10^{11}	3.86×10^{10}	7.23×10^{10}

Table 4. Numerical Data. Rectangular cylinder ($\epsilon_C = 1.8$, $L_D = 3\lambda$, *Noisy Case*). Computational indexes for different values of SNR .

	$f = 1\text{ GHz}$		$f = 2\text{ GHz}$	
	<i>IMSA - LS</i>	<i>Bare - LS</i>	<i>IMSA - LS</i>	<i>Bare - LS</i>
k_{tot}	506	69	532	200
f_{pos}	4.88×10^9	1.22×10^{11}	5.14×10^9	3.55×10^{11}

	$f = 3\text{ GHz}$		$f = 4\text{ GHz}$	
	<i>IMSA - LS</i>	<i>Bare - LS</i>	<i>IMSA - LS</i>	<i>Bare - LS</i>
k_{tot}	678	198	621	200
f_{pos}	6.55×10^9	3.51×10^{11}	5.99×10^9	3.55×10^{11}

Table 5. Experimental Data (Dataset “Marseille” [34]). Circular cylinder (“*dielTM_dec8f.exp*”). Computational indexes.